CRYSTAL GROWTH & DESIGN

pubs.acs.org/crystal

Article

Nanoscale Insights: Exploring Undersaturated Crystallization of Flufenamic Acid with Liquid Phase Transmission Electron Microscopy

Sara Fatima, Junbeom Park, Govind Ummethala, Shibabrata Basak, Rüdiger-A. Eichel, Amir Tavabi, Rafal Dunin Borkowski, Sarah Hudson, and Jennifer Cookman*

Cite This: *Cryst. Growth Des.* 2026, 26, 6261−6273

Read Online

ACCESS | Metrics & More | Article Recommendations | Supporting Information

ABSTRACT: Pharmaceutical crystallization traditionally requires supersaturation to occur and is typically monitored through macroscopic characterization methods that can measure induction times and growth rates. However, detailed insights revealing the precise steps and mechanisms of crystal nucleation and growth dynamics are lacking. This study explores the crystallization of a nonsteroidal anti-inflammatory drug, flufenamic acid, in undersaturated ethanol and isopropanol solutions using liquid phase transmission electron microscopy (LPTEM). LPTEM is a technique that provides real-time observations of nanoscale processes. Continuous electron-beam irradiation was found to induce nucleation and crystal growth at concentrations far below saturation. LPTEM can extract key kinetic parameters such as nucleation induction times and growth rates that inform and refine mechanistic models of crystallization. Due to the undersaturated nature of the crystallization conditions, these findings suggest newly discovered nucleation pathways, alternative to classical nucleation theory, revealing previously inaccessible mechanisms in crystallization of organic molecules.

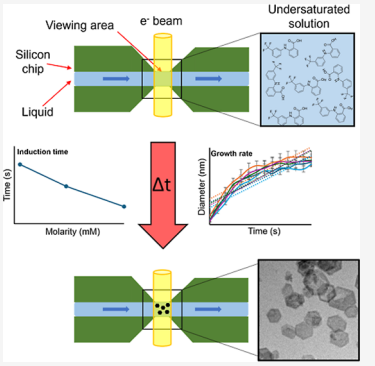

1. INTRODUCTION

Crystallization is an important step in pharmaceutical development, determining the purity, stability, and subsequent efficacy of active pharmaceutical ingredients (APIs) through control of key features such as polymorphism, solubility, and particle size. Uncontrolled crystallization has resulted in the commercial cessation of medications leading to notable restrictions in the industry's crystallization procedures.[1] One such example is rotigotine, a nonergot dopamine receptor stimulant recommended for the treatment of Parkinson's disease, which was temporarily withdrawn in 1998 due to polymorphic transformations limiting its transdermal patch performance.[2] Precise control of crystal form is essential, yet conventional, macroscopic crystallization methods even with in situ probes like FBRM or Raman offer limited nanoscale, real-time insights into nucleation and growth pathways, restricting mechanistic understanding and process control.

Regardless of crystallization technique, the final crystalline product is influenced by its environment, i.e., solvent,[3,4] saturation level,[5] vessel, temperature, mixing apparatus, etc.[6−8] Major pharmaceutical companies maintain dedicated crystallization departments to ensure robust product design, as regulatory bodies such as Food and Drug Administration (FDA) and the European Medicines Agency (EMA), set strict standards for pharmaceutical product safety and stability.[9−11] The nucleation,[12] growth behavior,[13,14] and subsequent final crystal product characteristics are particularly important to establish control over the process to comply with regulations. In situ characterization is required to unlock the precise crystallization mechanisms to fully understand the steps to achieve control over the nanoscale that influence the bulk material.

Rationalizing control over such processes begins by looking at the theories that govern them, such as classical nucleation theory (CNT)[15] and nonclassical crystallization (NCC).[16] These established theories assume supersaturation must be induced to allow crystallization to occur. However, neither CNT nor NCC can fully explain when this criterion is not met such as when crystallization occurs in undersaturated conditions, induced using electron beam irradiation.[17,18] An electron beam is known to interact with matter in a disparaging way, due to its ionization capability. When interacting with liquid, ionizing energy is predicted to trigger radiolysis of abundant molecules where the molecules are fractured and other radical, molecular, and gaseous species are created.[19] Seminal simulation studies have shown that the species generated through radiolysis can reach concentrations of >0.1 mM for water.[20] However, such studies have not been

Received: January 8, 2026
Revised: July 15, 2026
Accepted: July 16, 2026
Published: August 4, 2026

https://doi.org/10.1021/acs.cgd.6c00030
Cryst. Growth Des. 2026, 26, 6261−6273

conducted for other common solvents, such as ethanol (EtOH) or isopropanol (IPA). The influence of radiolysis has the potential to dramatically alter the local chemistry and offers the capability of modulating nucleation kinetics.[21] The detections of intermediate crystallization species, phase transitions, and the kinetics of chemical reactions are some of the important discoveries made possible by LPTEM predominantly in aqueous, inorganic, or metallic systems.[21] These revelations lead to a more profound comprehension of molecular dynamics in solution and crystallization mechanisms.[21]

Most LPTEM studies have focused on inorganic systems and studies on organic molecules are limited. Previous research by Cookman et al. demonstrated that electron beam-induced nucleation could initiate crystallization of an organic pharmaceutical ingredient, flufenamic acid (FFA), in undersaturated ethanol solutions (5 and 50 mM concentrations, corresponding to supersaturation (S) levels of 0.004 and 0.04, respectively, at 298 K). The observed hexagonal morphology was compared to Bravais Friedel Donnay Harker (BFDH) and attachment energy predictions for the Form I polymorph of FFA, which predicted a hexagonal morphology. FFA can crystallize in a variety of different solid forms. Lopez Mejias et al. employed low-temperature solid−solid transition and polymer-induced heteronucleation studies to obtain eight polymorphs of FFA (Forms I−VIII), along with a newly discovered Form IX, confirmed by PXRD and Raman spectroscopy (Table S1).[22] Nechipadappu et al. established that Form I is the most stable polymorph when crystallized from ethanol in slow evaporation tests under ambient conditions.[23] In contrast to the hexagonal morphology associated with Form I, Form III has been reported to preferentially form elongated, needle-like crystals.[22] These investigations underscore the complex polymorphism of FFA, particularly emphasizing the morphology characteristic of Forms I and III.

LPTEM presents a novel method for real-time observation of crystallization processes on the nanoscale, even in highly undersaturated conditions.[18] LPTEM differs from typical electron microscopy by enabling direct observation of dynamic processes in liquid environments with a high spatial and temporal resolution. With this ability, crystallization behaviors have been observed that defy traditional theories.[24] Cookman et al. proposed that beam-induced radiolysis of ethanol in LPTEM generates highly localized unique chemical environments that allow for nonequilibrium crystallization in undersaturated conditions by mechanisms independent of CNT or NCC pathways.[18] Building on this, the work presented herein studies the crystallization kinetics followed using LPTEM, of FFA in EtOH and IPA. Concentration-dependent observations are revealed, despite the severely undersaturated nature of all studied concentrations. By establishing control over the energy input, referred to as electron flux density (EFD) throughout, reproducible crystallization dynamics are observed, distinct for each solvent system. This study explores the impact of EFD, solvent choice, and concentration on crystallization under highly undersaturated conditions. This work not only challenges established crystallization theories but also positions LPTEM as a transformative tool for crystal engineering in pharmaceutical development.

2. EXPERIMENTAL SECTION

2.1. Materials

Flufenamic acid (FFA form I, 97%) was obtained from Thermo Scientific Ltd. Isopropanol (IPA, ≥99.95%), ethanol (EtOH, ≥95%), and toluene (≥99.8%) were sourced from Fisher Scientific. The Ocean holder assembly, comprising a calibration grid, chips, PEEK tubing, and O-rings, was acquired from DENSsolutions. FFA was recrystallized from toluene to obtain pure form III as confirmed by the reported literature.[25] All other chemicals and solvents were used as received without further purification.

2.2. Solubility Measurements Using the Gravimetric Method

Clean, dry vials (20 mL) were used to prepare samples for solubility measurements in EtOH and IPA. To minimize contamination, each vial was rinsed with 1 mL of the corresponding solvent before sample preparation. Subsequently, 2 mL of EtOH or IPA was added using a micropipette, followed by the addition of excess FFA (form III). A Teflon-coated magnetic stirrer was placed in each vial, which was then sealed with a lid and parafilm to prevent solvent evaporation and contamination, before being placed in a thermostatic water bath. Solubility was evaluated at 298.15, 303.15, 308.15, and 313.15 K in EtOH and IPA. A Grant TXF200 thermostatic circulating water bath (stainless steel, 38 L, stability ±0.005 K, uniformity ±0.02 K) with a serial magnetic stirrer maintained a constant temperature. The bath was preheated to the target temperature before sample placement and stirring was set at 700 rpm. Equilibration was allowed for 72 h to ensure saturation, after which stirring was stopped for 1 h to facilitate phase separation by filtration. The residual solid was analyzed via PXRD to determine the polymorphic form present at equilibrium. To prevent precipitation during filtration, 5 mL syringes, 0.20 μm syringe filters, and needles were preheated at 323.15 K for 15 min. Clean, preweighed vials were used for filtrate collection, with their empty weights (m_{empty}) recorded using a Mettler Toledo XP205 analytical balance (precision up to five significant figures). Filters were prewetted with the supernatant before filtration. The filtered solution was collected in preweighed vials, and the total mass ($m_{solution}$) was recorded. Solvent evaporation was conducted under a fume hood for 48 to 72 h, where the cap was left on loosely to avoid contamination, with residual drying in an oven at 333.15 K for 1 h to achieve constant dry weight (m_{dry}). Multiple weight measurements ensured complete solvent removal. Three replicates per temperature and solvent were done, totaling 24 vials per experiment (SI Section S2, Solubility Equations).

Each experiment was performed in triplicate, ensuring robust data collection with nine replicates per temperature. The as-received FFA, slurry residues, and final dried residual solids were characterized via powder X-ray diffraction (PXRD, Section 2.3).

2.3. Powder X-ray Diffraction

A thin layer of the crystals was placed on a zero-background disk. A diffraction pattern was obtained in the reflection mode with an Empyrean PANalytical diffractometer using a Cu Kα 1,2 radiation source (λ = 1.541 nm) operating at 40 mA and 40 kV. Using a step size of 0.05° and a scan speed of 0.034°/s, scans were carried out in the 2θ angle range of 5 to 40° (Figure S1).

2.4. LPTEM Experimental Setup

2.4.1. Sample Preparation. Solutions of FFA in EtOH (1, 5, 10, 50, and 100 mM) and IPA (5, 7.5, 10, 15, 20, and 50 mM) were prepared by dissolving the required amounts of FFA (Form III) and stirring at room temperature until complete dissolution. The solutions were filtered using 0.2 μm PTFE syringe filters to remove any undissolved particles. A controlled volume of each filtered solution was flowed into the liquid cell (described below) using PEEK tubing, ensuring an air-free environment. The liquid cell was sealed immediately after loading to prevent evaporation and contamination.

2.4.2. LPTEM Holder Preparation. FFA solutions were analyzed using a Thermo Fisher Scientific (TFS) TEM compatible DENSsolutions Ocean holder fitted with a nanocell comprising two

https://doi.org/10.1021/acs.cgd.6c00030
Cryst. Growth Des. 2026, 26, 6261−6273

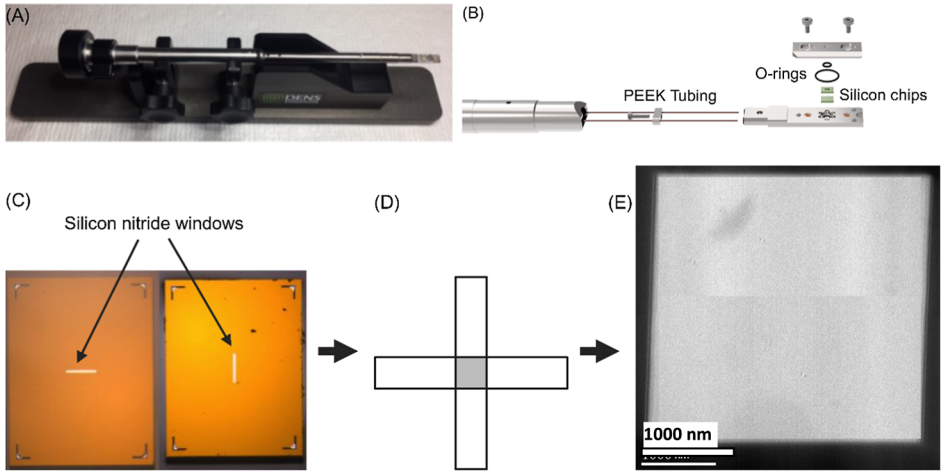

Figure 1. Schematic of different aspects of the LPTEM setup (A) the DENSsolutions Ocean holder; (B) expanded view of the holder tip; (C) optical image of the silicon chips indicating the silicon nitride; (D) orthogonal arrangement of the windows; and (E) TEM micrograph of the square silicon nitride electron transparent viewing area.

silicon chips, each with a window of silicon nitride, an electron-transparent material. The chips were plasma-cleaned in a Gatan model 950 Advanced Plasma System for 5 min to render the surfaces hydrophilic, then arranged orthogonally so the windows crossed (Figure 1). For a 1 mm × 1 mm window and a 200 nm spacer, the enclosed volume is ∼200 pL. The assembled holder was leak-tested on a Pfeiffer HiCUBE ECO vacuum pump. The holder was considered successfully hermetically sealed and appropriate to be subjected to the high vacuum of the TEM, if the vacuum could reach $\times 10^{-6}$ mbar in less than 10 min. For the TEM calibration protocol used, refer to SI: Section S4.

2.4.3. LPTEM Experimental Protocol. The PEEK tubing was inserted through the holder, and O-rings were positioned at both the inlet and outlet ends before securing them with screws. The rear end of the holder was sealed by using blue flanges, and a small O-ring was placed at the base of the hollow chamber. The assembled tip of the holder (Section 2.4.2) was mounted and fixed with screws. The assembly was inspected to confirm the integrity of the seals and the structural stability of the components. Prior to introducing the FFA solutions, the optical integrity of the chips was examined under a polarized light optical microscope to ensure the absence of defects.

For solution flow experiments, PEEK tubing was connected to a 5 mL Luer lock syringe containing the respective solvent (EtOH/IPA), which was delivered via a syringe pump at 25 μL/min. The window location was mapped using the TEM software, and the quality of the liquid environment was assessed before introducing the FFA solution. The prefiltered FFA solutions were loaded into the syringe pump, connected to the Ocean holder PEEK tubing, and flowed at a controlled rate of 25 μL/min. The flow was stopped before exposure to the beam. The solution was then exposed to the electron beam under controlled dose conditions while monitoring crystallization events in real time with initial exposures of ∼120 s in IPA and ∼15 s in EtOH. The solution was further exposed to the calibrated electron flux for both the systems allowing the crystals to grow. All experiments were conducted under identical conditions to ensure reproducibility, and observations were recorded to analyze nucleation and growth behavior under varying solution concentrations. Unless otherwise stated, all the images presented in this manuscript are from the viewing window.

2.5. TEM Operation and Electron Flux Density Quantification

All experiments of FFA in EtOH were conducted at the Ernst Ruska-Centre for Microscopy and Spectroscopy with Electrons in Jülich, Germany. A TFS Titan TEM equipped with a Schottky field-emission gun operating at 300 kV was used to acquire the data. Electron flux density was controlled by varying the C2 lens and measured with a Gatan K2 Summit direct electron detector and data directly acquired using the same detector.

All experiments of FFA in IPA were conducted in the Bernal Institute, University of Limerick, Ireland on a TFS Titan TEM operating at 300 kV. The Gatan K2 Summit direct electron detector was setup in the counting mode to calibrate the settings required for the selected electron dose range. Image and video recordings were completed using the Gatan OneView CMOS camera for improved contrast and manageable framerate. The exact number of electrons striking the material in a specific location was determined using the counted mode of the K2 Summit Direct Electron Detector to estimate the electron flux ($e^-/Å^2/s$) as mentioned in Table S2. Counting individual electrons as they hit the sensor is made possible by a separate processing unit within the camera. The settings recorded were the monochromator value, beam diameter, and flu screen electron flux readout. While adjusting the monochromator value using the control panel knob, the electron flux ($e^-/Å^2/s$) was measured, with a ±1 increment. This was to account for the sensitivity of the knob when changing the arbitrary value. After optimizing the in situ data acquisition parameters, the flux measurements were finished. The settings were replicated to correspond with the real measurement conditions utilized during sample crystallization under electron beam monitoring to ascertain the electron flux. The electron flux at the sample is controlled by the monochromator slit setting. Opening the monochromator (larger slit) increases flux, whereas closing it (smaller slit) reduces flux. The dependence is strongly nonlinear (approximately exponential) over the useable range.

2.6. Induction Time Measurements

In LPTEM experiments, induction time is measured by recording the process from the beam's onset until the visible onset of nucleation. The prepared solutions were loaded onto the silicon nitride windows with no spacers. This ensured that the liquid layer is thin enough (∼200 nm) allowing the passage of electrons. The window was further exposed to the beam and recorded at a frame rate of 100 frames per second (fps). These recorded videos were further analyzed to assess the time intervals from the beam onset to the appearance of the first crystal nuclei (the induction time).

2.7. Methodology for Manual Measurement of Growth Rate

For the growth rate of crystals to be analyzed, 20 crystals were selected per frame, and size was manually measured as two measurements at 90 deg to each other for each particle and averaged to estimate the growth rate (nm/s) at 10 s intervals using a Digital Micrograph (Gatan Microscopy Suite, GMS 3). The measurements were made retrospectively, beginning in the last frame (frame before crystal degradation starts), where the crystals were detectable and

https://doi.org/10.1021/acs.cgd.6c00030
Cryst. Growth Des. 2026, 26, 6261−6273

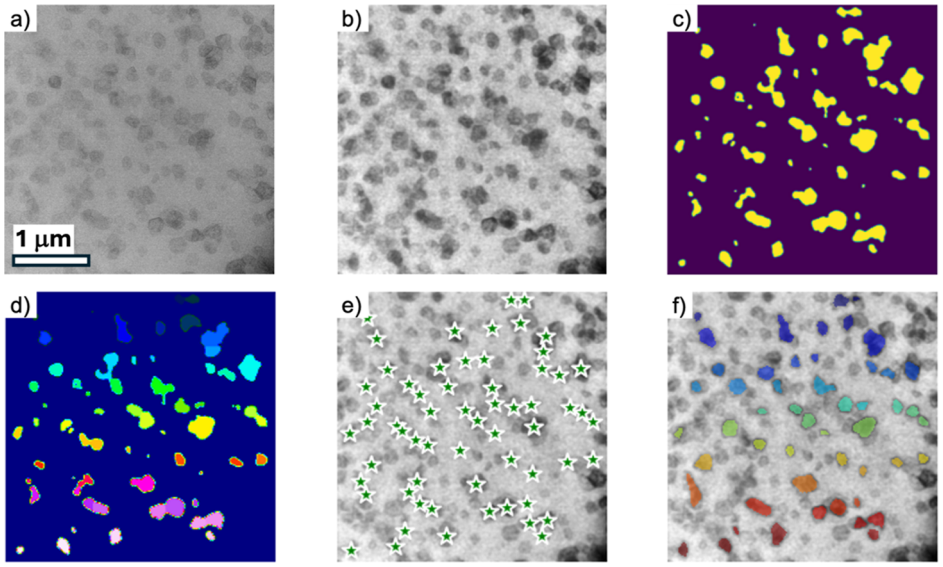

Figure 2. A scheme of the image processing workflow: (a) Original TEM micrograph; (b) Gaussian filter (to denoise) and histogram equalization (to enhance contrast); (c) thresholding (to separate particles from the background); (d) watershed (to distinguish overlapping particles); (e) central locations of detected particles; and (f) segmented particles using a Deep learning method (Meta-SAM model[26]).

working backward to their first detectable appearance to measure the onset of growth precisely. The size data gathered were plotted on Origin to produce growth curves. The growth rate of a crystal was determined by using the slope of the linear fit. The final reported growth rate is the average of the individual slopes calculated for all 20 crystals in one set of data.

2.8. Growth Rate Measurement Using Deep Learning-Based Segmentation

To measure the growth rate using deep-learning-based segmentation, a particle size distribution (PSD) was obtained from each TEM micrograph. This was achieved using a six-step image processing method (Figure 2). The original 4 k TEM image was first rescaled to 1 k and normalized. Next, a Gaussian filter and histogram equalization were applied to denoise and enhance image contrast. Thresholding was then used to presegment particles from the background. The watershed method was applied to distinguish overlapping particles, followed by listing the center locations of the presegmented particles. Finally, the Meta-Segment Anything Model (SAM) was used to segment particles from each center location.[26] The PSD was collected by measuring the area of the segmented particles and converting it to the diameter using the assumption of a circular shape. Particles larger than 50% of the image area and smaller than 1% were ignored. These steps were applied to each TEM image in a data set repeatedly, and the collected PSDs were merged into a single result data set. The growth rate was then calculated by performing linear regression on the average particle diameter per TEM image and the capture frame time of the TEM image. A boxplot from the result data set provided statistical assessments.

3. RESULTS AND DISCUSSION

The aim of this study was to elucidate the crystallization behavior of FFA under undersaturated conditions using LPTEM, regarding solvent type, concentration, and electron beam energy input. By comparing crystallization events in ethanol (EtOH) and isopropanol (IPA), we investigated the extent to which solvent-specific properties influence beam-induced nucleation, induction times, growth kinetics, and polymorphic outcomes. This section presents a detailed analysis of solubility measurements, crystallization phenomena observed via LPTEM, and the influence of electron flux density on crystallization kinetics. These findings are used to propose new mechanisms of crystal formation that are relevant to pharmaceutical systems.

3.1. Solubility Baselines and Undersaturation Criteria

Traditional solubility experiments were conducted to establish a benchmark for evaluating the degree of undersaturation applied in this study. The mole fraction solubility of FFA in IPA was determined to be 0.069 ± 0.012 at 298 K, corresponding to a saturation concentration of 0.97 ± 0.17 M. This solubility was slightly lower than previously reported solubility data for FFA in IPA (1.39 M).[27] The mole fraction solubility of FFA in EtOH was determined to be 0.064 ± 0.010 at 298 K. This corresponds to a saturation concentration of 1.20 ± 0.18 M. This solubility was similar to previously reported solubility data for FFA in EtOH (1.25 M).[18] The concentrations investigated herein were significantly below the determined solubility limits. The concentration range was designed to expand on a previous work carried out by Cookman et al. in EtOH and then compared to in a new solvent system, i.e., IPA, in a similar undersaturated solute concentration range.

3.2. LPTEM—Electron Flux Modulation

Crystallization under the beam of FFA solutions in both solvents were initially tested across concentrations 1−100 mM at an electron flux density (EFD) range of 1−10 $e^-/Å^2/s$ (further described in the following paragraph). Nucleation was observed at all FFA-EtOH concentrations tested in this range, but no nucleation events were observed at FFA concentrations of 1, 5, and 7.5 mM in IPA. Additionally, at higher concentrations (≥50 mM), the solvent in the FFA-IPA solution was repeatedly displaced from the window, prohibiting observation of liquid phase phenomena (Figure S2). Therefore, the chosen concentrations for analysis in IPA were 10, 15, and 20 mM and in EtOH were 1, 5, 10, 50, and 100 mM.

Initially, the influence of EFD on the crystallization of FFA was explored to establish the minimum energy input required for nucleation to occur and crystals to remain stable. For the IPA solutions, it was found that by incrementally increasing the

https://doi.org/10.1021/acs.cgd.6c00030
Cryst. Growth Des. 2026, 26, 6261−6273

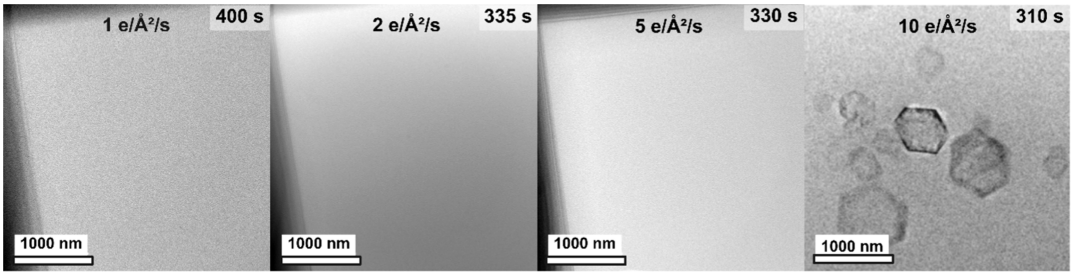

Figure 3. Micrographs displaying the irradiation of a solution of 10 mM FFA in IPA with time stamps for duration of exposure to beam. The lack of nucleation events can be seen at EFDs of 1, 2, and 5 $e^-/Å^2/s$, and an example of identified hexagonal crystals induced at 10 $e^-/Å^2/s$.

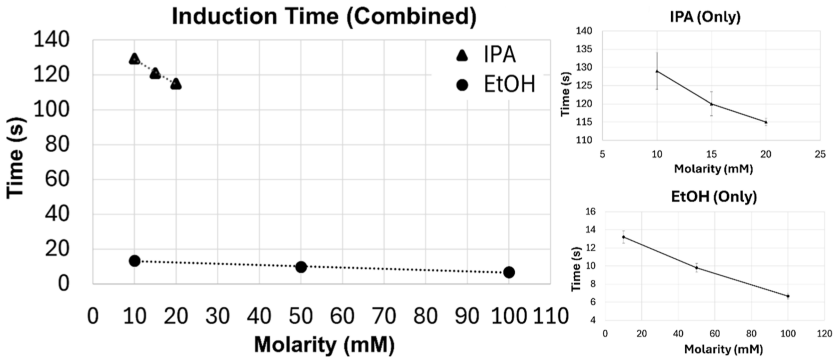

Figure 4. Nucleation induction time plotted against concentration in molarity for FFA in IPA and in EtOH. In both cases, the induction time decreases with increasing molarity. EFD: 10 $e^-/Å^2/s$ (IPA) and 1 $e^-/Å^2/s$ (EtOH).

EFD to 1, 2, and 5 $e^-/Å^2/s$ (Figure 3) nucleation events were not initiated, irrespective of the concentrations tested within this study. EFDs higher than 10 $e^-/Å^2/s$ caused irreversible effects to the solvent, displacing it from the windows (Videos S1, S2, and S3). In addition, at EFDs higher than 10 $e^-/Å^2/s$, there was significant energy transfer to the solvent, which was suspected to produce localized heating and extensive radiolysis. These effects together can remove IPA from the viewing area through gas evolution and thermal disturbances. Therefore, 10 $e^-/Å^2/s$ was the optimum electron flux for studying FFA crystallization in IPA solutions (Figure 3). For EtOH, the minimum EFD required to initiate nucleation events was 1 $e^-/Å^2/s$. EFDs up to 10 $e^-/Å^2/s$ also initiated nucleation, however, we aimed to control the minimum energy input required and therefore chose 1 $e^-/Å^2/s$ as the EFD for all EtOH concentrations.

To ensure that the observed nucleation events required the FFA solutions and were not caused by the solvent itself, the solvent alone was subjected to continuous irradiation at the tested EFDs for >5 min (Figure S3). No nucleation events were observed, confirming that the FFA was required in the solution for nucleation to occur, despite the undersaturated conditions.

It is postulated that solvent tolerance to the electron beam is responsible for the 10-fold decrease in the required EFD for nucleation to occur in EtOH compared to IPA. On a fundamental level, the bulk properties of the solvents can indicate its tolerance to decomposition mechanisms, e.g., the boiling point of EtOH (78.23 °C) is lower than that of IPA (82.6 °C), suggesting that EtOH would be more volatile that IPA. Although the influence of bulk-scale properties is relevant to consider, in LPTEM experiments, it is important to recognize that solution radiolysis due to the ionizing irradiation from the electron beam can occur and greatly influence the experiments and observations. Due to the abundance of LPTEM studies in aqueous solutions, a significant body of work has been published on the radiolysis of water including simulation studies on the predicted quantities of each radiolysis product with continuous irradiation.[28,29] The trends discovered from these studies can be used to rationalize the nanoscale radiolysis of nonaqueous solvents in LPTEM. For example, in a report from Fritsch et al., simulation experiments illustrated that radiolysis products from water such as H_2, O_2, H_2O_2, and OH^- reached up to mM in concentration with continuous irradiation.[20] This knowledge when linked with crystallization suggests that when nucleation of FFA occurs in LPTEM, the pure mother solvent likely reduces in quantity, giving way to a multicomponent solvent composed of other stable molecular products created in the radiolysis process. In the case of EtOH, molecular products created are expected to be acetaldehyde (CH_3CHO), hydrogen peroxide (H_2O_2), and 2,3-butanediol ($(CH_3CHOH)_2$),[30,31] and for IPA, the molecular products expected are acetone ($(CH_3)_2CO$) and water (H_2O), as a result of reactions with produced radicals of IPA ($^{\bullet}R-OH$), methane ($^{\bullet}CH_3$), and hydroxyl ($^{\bullet}OH$).[32,33]

It can be hypothesized that the electron beam alters the local solution chemistry, generating a driving force that enables the system to overcome the nucleation energy barrier, ultimately leading to the crystallization of a phase that closely resembles the metastable polymorph of FFA. The unique crystallization conditions to reach local supersaturation in apparent undersaturated conditions are further explored in the following sections to begin to rationalize the mechanisms at play and how they compare to the conventional understanding of crystallization.

3.3. Nucleation Induction Time

The electron beam, as previously mentioned, acts as an external energy input, introducing localized changes to the

https://doi.org/10.1021/acs.cgd.6c00030
Cryst. Growth Des. 2026, 26, 6261−6273

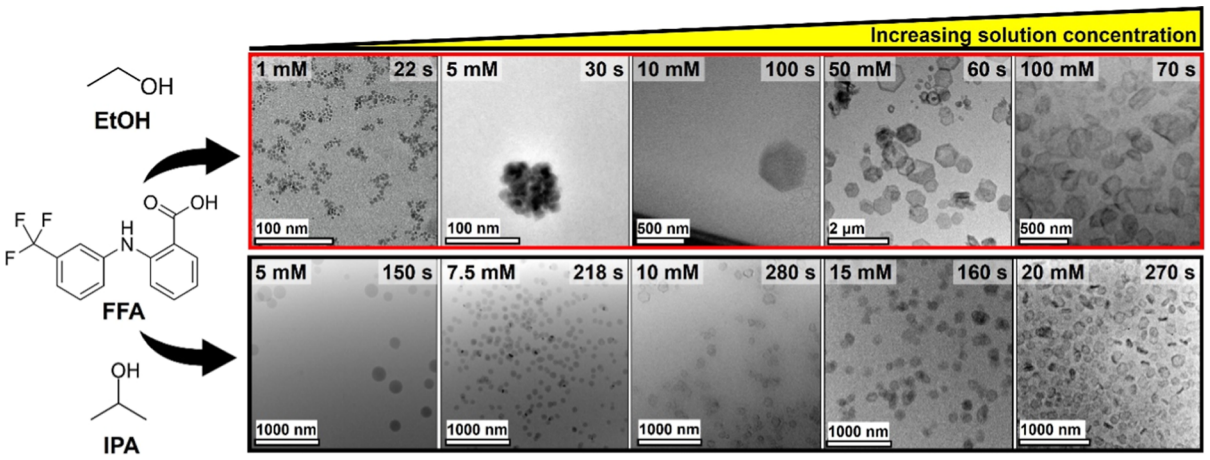

Figure 5. Example micrographs from LPTEM experiments to summarize the formed FFA features in EtOH and IPA solutions at concentrations of 1, 5, 10, 50, and 100 mM (EtOH) and 5, 7.5, 10, 15, and 20 mM (IPA). In both systems, concentrations >10 mM displayed hexagonal and other faceted features, whereas <10 mM displayed droplet-like or nanoparticle features. EFD: 1 $e^-/Å^2/s$ for EtOH and 10 $e^-/Å^2/s$ for IPA; time stamps = induction time + growth time.

solution and driving it from undersaturation to supersaturation, facilitating nucleation. Due to the undersaturated nature, the electron beam irradiation relies on creating the nucleation events, whether through the radiolysis of the solvent and subsequent interactions or another undiscovered mechanism. To gain more insights into the nucleation process, the induction time is evaluated based on the time taken from initial electron beam exposure to the detection of the first visible nuclei. In this context, assessing the induction time depicts how fast the nucleation happens in an undersaturated system based on the concentration and solvent used.

From Figure 4, it can be observed that increasing the concentration from 10 to 20 mM (in IPA) and 10 to 100 mM (in EtOH) resulted in a corresponding decrease in the induction time. This is according to the classical theory of nucleation that higher levels of supersaturation yield a reduced nucleation energy barrier, and therefore an increased rate of crystallization.[34] Notably, this behavior is sustained in LPTEM demonstrating that despite highly undersaturated conditions and beam effects in LPTEM, the system continues to exhibit a linear dependence on concentration in response to nucleation kinetics. This suggests that while the beam is a nonequilibrium energy input, it retains basic thermodynamic driving forces for nucleation.

3.4. LPTEM Crystallization Observations

Electron beam-induced crystallization of FFA in EtOH previously demonstrated that primarily hexagonal features developed at a concentration of 50 mM.[18] Furthermore, nanoparticles without any observable facets were observed to form in an EtOH−H_2O-mixed solvent system.[17] One of the goals of this current study was to determine how far below the solubility limit nucleation could still be initiated with electron-beam irradiation, effectively assessing the sensitivity of the LPTEM system to subtle changes in solute concentrations. In doing this, it was found that there were concentration-dependent observations of formed features, despite all conditions being undersaturated, as low as S = 0.0008 (1 mM in EtOH) (Figure 5).

In both solvent systems, hexagonal and other faceted features developed at concentrations higher than 10 mM, accompanied by an increase in the number of nucleated features. As the concentration increased, a higher number of smaller hexagonal particles were observed, with a reduced induction time (Figure 4), indicating greater nucleation rates (Videos S4, S5, S6, S7, and S8). In the EtOH system, all tested concentrations above 10 mM resulted in hexagonal crystals. However, in the IPA system, while the dominant morphology was hexagonal, deviations were observed at the highest concentration of 20 mM. For instance, at 20 mM, morphologies such as truncated triangular, elongated hexagonal, and asymmetric hexagonal features were observed (Figure 5).

Below 10 mM, both solvent systems showed clusters and particles without visible edges of facets, suggesting the absence of mature crystals that can be explained by nonclassical theories like the prenucleation cluster theory[35] or nonclassical crystallization theory.[17,34] In the EtOH system, nanoparticles of approximately 8 nm were observed at 1 mM. Further increasing the concentration to 5 mM resulted in dynamic clustering of nanoparticles upon continued irradiation up to ∼200 s. These clusters varied in size depending on the number of nanoparticles contained in the aggregate. Intercluster interactions were also observed, where clusters in proximity appeared to join to form larger aggregates (Videos S9 and S10). For the IPA system, concentrations less than 10 mM displayed low density, unstructured features resembling droplet-like formations described in nonclassical crystallization, also known as mesoscale clusters.[36,40] This was particularly evident at 5 mM, while at 7.5 mM, some structured faceting could be seen. Additionally, the presence of high-density nanoparticle aggregates like those observed in the FFA-EtOH system was observed. This variation in resultant features demonstrates that even modest concentration changes in undersaturated solutions significantly impact crystallization behavior. This highlights the ability of LPTEM to facilitate the observation of pathways that are noncompliant with conventional saturation-based models, such as CNT.

The ability of the system to nucleate at these low concentrations underlines the significant role of electron beam irradiation in triggering crystallization through a nonclassical, beam-mediated mechanism. As previously reported, a hexagonal morphology was observed, consistent with Form I of FFA. This morphology aligns with earlier

https://doi.org/10.1021/acs.cgd.6c00030
Cryst. Growth Des. 2026, 26, 6261−6273

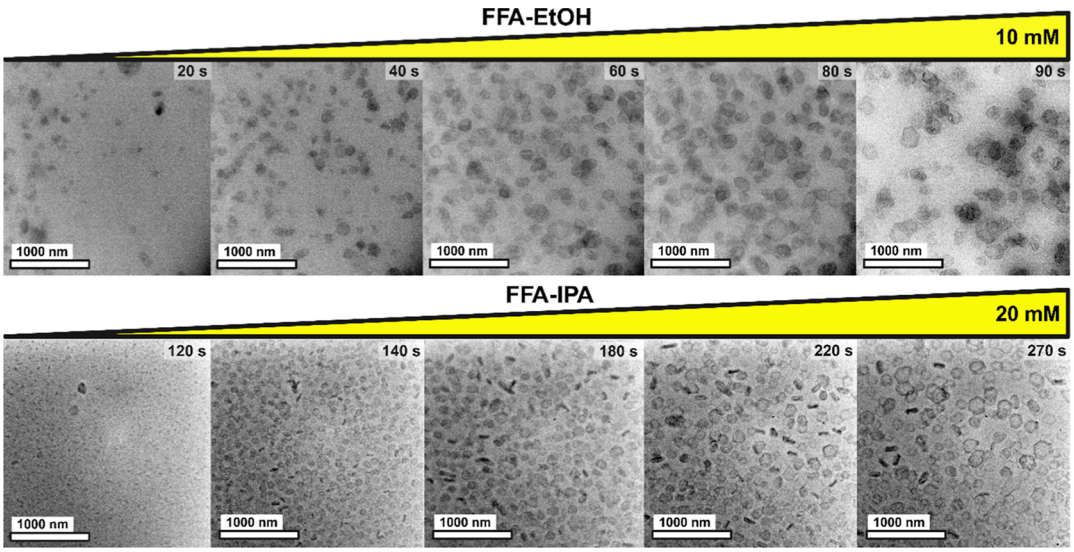

Figure 6. Formation of nuclei and subsequent growth into hexagonal crystals in the EtOH and IPA systems at concentrations of 10 mM and 20 mM, respectively. EFD: 1 $e^-/Å^2/s$ (FFA-EtOH) and 10 $e^-/Å^2/s$ (FFA-IPA); time stamps = growth time−induction time; see also Videos S4, S5, S6, S7, and S8.

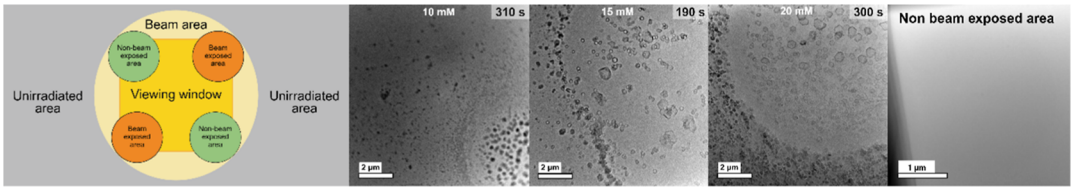

Figure 7. Crystals inside and outside the beam area indicating that solvent-mediated crystallization (crystallization induced by the diffusion of the solvent's radiolysis products outside the beam area) mechanism dominates in the nonirradiated regions. System: FFA-IPA; Mag: 2 μm; electron flux: 10 $e^-/Å^2/s$; time stamps = induction time + growth time + further exposure to the beam.

studies that have identified hexagonal crystal habits as a characteristic of Form I.[18] No needle-like crystals were observed in this study, which are more typical of Form III, the thermodynamically stable form at room temperature (stable below 315 K) and the equilibrium phase under ambient conditions.[25,37,38]

3.5. Continuous Electron Beam Irradiation

Thus, nucleation in FFA-IPA and FFA-EtOH solutions occurs at highly undersaturated levels when subjected to electron beam irradiation. A minimum exposure duration of ∼120 s was required for the FFA-IPA system to observe nucleation, since no nucleation events were detected at shorter exposure times whereas only ∼15 s exposure duration was required for the FFA-EtOH system.

With prolonged irradiation with the electron beam, the pre-existing hexagonal features displayed continued growth (Figure 6) alongside the emergence and subsequent enlargement of new nuclei into hexagonal crystals. These structures exhibited strong mass−thickness contrast with well-defined, faceted edges, a characteristic of crystalline materials. Both the existing crystals and newly formed nuclei underwent analogous processes, characterized by linear growth trends under sustained irradiation (Section 3.7). The formation of hexagonal crystals (Figure 6) strongly suggests the growth of form I FFA, consistent with previous EtOH-based studies at 50 mM.[17] A similar result was observed for IPA. Because of the challenges associated with acquiring electron diffraction in thick liquid environments, it was not possible to acquire electron diffraction in each instance.

These findings collectively highlight the nature of beam-induced crystallization, which is solvent-dependent and concentration-dependent, and challenge the premise that classical nucleation theory needs bulk supersaturation to form crystals. The observed differences arise from the combined physicochemical and radiolytic properties of both solvents during the radiolysis. Under the imaging conditions employed here, EtOH showed a more pronounced beam-induced chemical response than IPA, evidenced by a shorter time-to-threshold for nucleation and crystallization at lower electron flux density. Rather than arising from solvent volatility, this behavior is attributed to the beam-driven radiolysis processes under these conditions, including the generation, recombination, scavenging, and transport of radiolysis species. The resulting transient perturbation of local solution chemistry can shorten the time-to-threshold for nucleation, thereby enabling crystallization even though the bulk solution remains globally undersaturated. In contrast, IPA appears to require a larger beam-induced perturbation before nucleation occurs, consistent with a higher flux threshold for crystallization.

These observations are in accordance with the hypothesis that crystallization under conditions of undersaturation is aided by localized changes induced by the electron beam temporarily enhancing local supersaturation.

https://doi.org/10.1021/acs.cgd.6c00030
Cryst. Growth Des. 2026, 26, 6261−6273

Table 1. Difference in Induction Times and Manual Growth Rates of FFA in Two Solvents: EtOH and IPA at Set Electron Fluxes and Different Saturation Levels Based on Their Respective Solubilities at 298 K (n = 3)

solvent	solute concentration (mM)	S ratio	electron flux ($e^-/Å^2/s$)	induction time (s)	growth rate (nm/s)	growth time (s)
EtOH	10	0.008	1	13 ± 1	1.86 ± 0.45	102 ± 3
EtOH	50	0.04	1	9 ± 2	7.25 ± 0.31	61 ± 2
EtOH	100	0.08	1	6 ± 1.5	13.83 ± 3.5	72 ± 2.5
IPA	10	0.010	10	129 ± 2	4.06 ± 1.35	151 ± 9
IPA	15	0.015	10	121 ± 3	2.72 ± 1.20	39 ± 1.5
IPA	20	0.020	10	115 ± 2.5	1.08 ± 0.19	155 ± 5

3.6. Crystal Growth Outside the Beam Area

FFA was observed to crystallize within and outside the electron beam area, where the crystals outside the beam area were smaller in size than the crystals within the beam. It is proposed that prolonged exposure of the electron beam within the zone of irradiation promotes further growth of the crystals, resulting in the observed difference in size, as evident from Figure 7. In this system, we hypothesize that the electron beam acts as an external stimulus that initiates nucleation and promotes a shift from a nucleation-dominated regime to one in which crystal growth becomes more prominent. Under these unique crystallizing conditions, this behavior is most likely associated with radiolysis-induced changes in local solution chemistry within the irradiated volume, while beam heating or evaporation are considered secondary unless independently quantified.[39,40] The resulting behavior can be rationalized by an initial transient increase in the local driving force that triggers nucleation of a limited number of nuclei, followed by local solute depletion around these nuclei, which suppresses further nucleation and reduces nucleus number density. Continued irradiation then preferentially sustains growth and coarsening of existing crystals through ongoing reaction-diffusion/transport in the beam-exposed region, yielding fewer but larger crystals with prolonged exposure.

On the other hand, outside the beam area, the absence of the aforementioned effects results in slower growth and diffusion-based crystallization. This leads to the formation of smaller crystals, as the system relies on the radiolysis products diffusing out for diffusion-mediated crystallization without the beam's catalytic influence (Figure 7). Schneider et al. and Fritsch et al. highlight the impact of beam-induced radiolysis in altering the chemical environment when using liquid-phase TEM. Radiolysis products such as H^+, OH^-, and H_2O_2 diffuse out from the irradiated zone due to steep concentration gradients and create spatially distributed chemical effects.[28,39] Fritsch et al. proceed to emphasize that such off-beam reactive species propagation complicates quantitative interpretation in LPTEM, as unexposed regions may be affected by unwanted reactions such as crystallization, initiated by the diffusive outgrowth of radiolysis products.[39]

3.7. Assessing Growth Rates

By leveraging real-time imaging and controlled electron flux along with concentration conditions, it was possible to measure growth rates (within the beam area) and reveal the growth kinetics and morphological evolution at the nanoscale.

Differences in solubility between EtOH and IPA and the resulting solution concentrations, lead to variations in nucleation behavior and crystal growth rates. In addition to these concentration effects, the susceptibility of each solvent to radiolysis also influences the crystallization dynamics, together determining the observed differences in nucleation and growth under the experimental conditions. The FFA particles exhibited linear growth from nucleation in both solvents. Growth rates of 1.86 ± 0.45 nm s^{-1} (10 mM), 7.25 ± 0.31 nm s^{-1} (50 mM), and 13.83 ± 3.50 nm s^{-1} (100 mM) were observed in the FFA-EtOH system (Table 1; Figure S5). At 50 mM, the rate observed in this work was ∼34% higher than the ∼5.4 nm s^{-1} reported by Cookman et al. in EtOH, where the EFD control was not consistently controlled.[17] For the FFA-IPA system, the growth rates showed an unexpected decrease with increasing concentration (Table 1; Figure S5). This deviation from classical growth trends can be explained by the solute depletion mechanisms.[41]

At lower concentrations in IPA (10 mM and 15 mM), the available solute molecules readily participated in crystal growth, maintaining a relatively high growth rate. A greater rate of nucleation events is encouraged by the solutions with higher concentrations such as 20 mM. The solute supply for each developing crystal is depleted more quickly because of these nuclei competing for the available solute molecules in the solution, which causes slower individual crystal growth rates (Figure S6). This trend is consistent with diffusion-limited growth models, where an increase in nucleation events depletes local solute availability, thereby slowing down overall crystal growth, which has also been hypothesized for the crystals formed outside the beam area in this study. According to Cookman et al., these dynamics are visible for FFA in solvent-mediated crystallization under TEM, where competition can result in smaller crystals because of high nucleation rates in localized supersaturated conditions (such as under beam-induced effects).[17]

The distinct growth rate trends in the two solvents suggest that solvent physical and chemical properties along with molecular interactions and concentration play a crucial role in dictating crystallization behavior. Ethoxy radicals, acetaldehyde, and H^+ are produced when EtOH is irradiated, leading to localized acidification of the area.[30] It is hypothesized that the pH drop somehow affects the ionization of FFA, altering solubility and promoting nucleation in undersaturated concentrations.[18] Due to the more simplistic molecular structure, EtOH is more prone to radiolytic breakdown.[30] IPA, having a branched structure, produces acetone and isopropyl radicals[19] but because of its higher stability under the beam, allowing for slower crystallization. These findings highlight how solvent choice significantly influences the nucleation and growth of FFA crystals, as EtOH and IPA exhibit differing susceptibilities to beam-induced effects and radiolysis. EtOH tends to maintain more stable growth environments under irradiation, while IPA is more prone to radiolytic degradation, leading to enhanced nucleation and diffusion-limited growth. In an effort to explain the growth mechanism, we explored a Wagner/LSW-style analysis by converting the 2D-projected platelet growth to a thickness-

https://doi.org/10.1021/acs.cgd.6c00030
Cryst. Growth Des. 2026, 26, 6261−6273

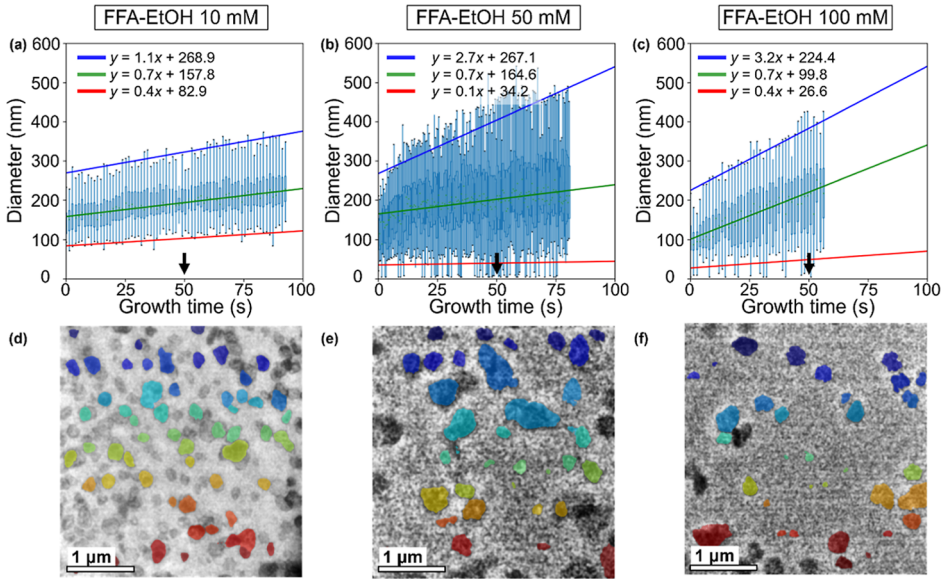

Figure 8. Automated particle size measurement results of FFA-EtOH solutions at 10, 50, and 100 mM: (a−c) Boxplot and fitting lines and (d−f) detected particles overlaid on contrast enhanced TEM image at 75 s. Statistical measurements illustrated in the figure: Green line represents 50% (medium-sized particles), blue line denotes 99% (largest-sized particles), and red line reflects 1% (smallest or nongrowing particles). System: FFA-EtOH: (a) 10 mM, (b) 50 mM, and (c) 100 mM; Electron flux: 1 $e^-/A^2/s$. The *x*-axis represents the growth time, which is the time after induction. The downward-pointing arrow indicates the time points of the respective images in the figure.

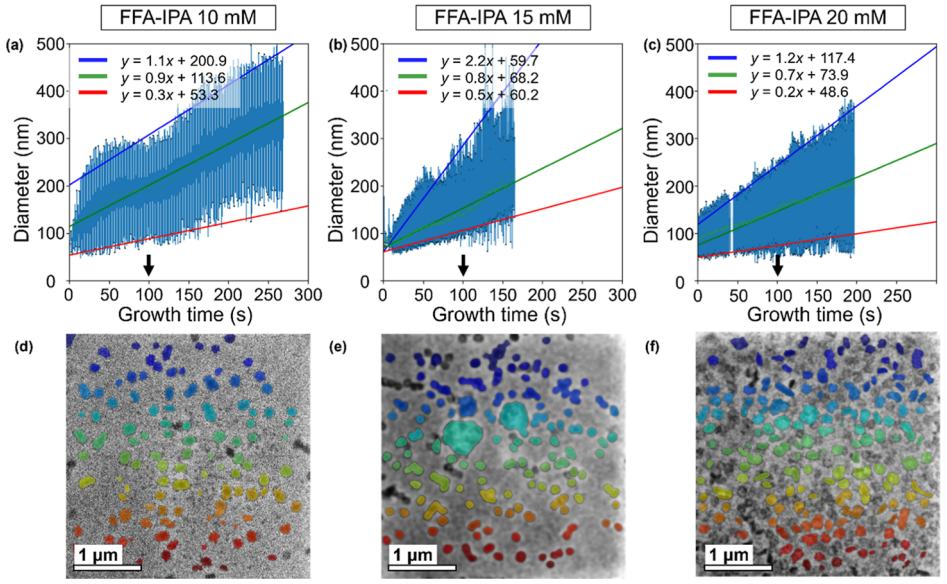

Figure 9. Automated particle size measurement results of FFA-IPA 10, 15, and 20 mM. (a−c) Boxplot and fitting lines and (d−f) detected particles overlaid on contrast enhanced TEM image at 150 s. Statistical measurements illustrated in the figure: Green line represents 50% (median), blue line denotes 99% (largest population), and red line reflects 1% (smallest population). System: FFA-IPA: (a) 10 mM; (b) 15 mM; and (c) 20 mM; Electron flux: 10 $e^-/A^2/s$. The *x*-axis represents the growth time, which is the time after induction. The downward-pointing arrow indicates the time points of the respective images in the figure.

based volume and a spherical-equivalent radius. However, as our crystals are anisotropic platelets (and tracking begins from finite, nonzero sizes for some concentrations in EtOH), the underlying spherical assumptions are not valid, so this approach was not used for a mechanistic interpretation in this system.[42]

Under prolonged electron beam irradiation in both solvents, the initially formed FFA crystals are susceptible to structural degradation caused by solvent displacement and the solvent's resilience to the beam (Video S11). This is attributed to cumulative action of radiolysis, localized warming, and prolonged solvent evaporation, all of which destabilize the crystallization environment. Beam-induced fragmentation in certain cases results in crystal etching, particularly at high flux densities or long durations (Video S11). These results highlight the importance of controlling exposure time to capture growth dynamics without sacrificing structural integrity. All the images shown in this manuscript are from before any fragmentation had occurred.

3.7.1. Growth Rate Calculation Using Deep Learning. The deep-learning-based segmentation approach was employed to quantify growth rates across different concentrations

https://doi.org/10.1021/acs.cgd.6c00030
Cryst. Growth Des. 2026, 26, 6261−6273

and dose rates for flufenamic acid in ethanol. A segment anything model (SAM),[26] combined with prelabeling using thresholding and watershed segmentation, provided an improved framework for tracking individual particles over time. Growth rates were extracted by analyzing particle diameter progression across successive frames. The growth time (on the *x*-axis) in Figures 8 and 9 represents the additional exposure to the beam after the induction period.

For 10 mM FFA-EtOH solutions, the particles display steady but slow growth (Figure 8a,d). Linear fits to the automated tracks give slopes of ∼0.7 nm s^{-1} for the median cohort (green) and ∼1.1 nm s^{-1} for the fastest 99th-percentile particles (blue). Diameters approach ∼310 nm at 50 s within the observation window for more than 99% of the population. The population remains broad, with a persistent first-percentile tail (red) of small or nongrowing particles, indicating growth even at low supersaturations. For 50 mM, growth accelerates and becomes more heterogeneous (Figure 8b,e). The fastest cohort grows at ∼2.7 nm s^{-1}, while the median remains ∼0.7 nm s^{-1}. 99% of the particles from 50 mM solution are ∼390 nm or smaller at 50 s. Transient plateaus and bursts are evident in individual traces, suggesting intermittent replenishment and/or beam-modulated chemistry. The separation between the blue (rapid) and green (median) envelopes widens relative to 10 mM, consistent with a minority of particles accessing locally relatively higher supersaturation levels. For 100 mM, growth is mostly continuous and rapid (Figure 8c,f). The 99th-percentile envelope yields a growth rate of ∼3.2 nm s^{-1}, and the median advances to ∼2.4 nm s^{-1}. 99% of the particles from 10 mM solution are ∼410 nm or smaller at 50 s. A larger fraction of particles occupies the upper (blue) envelope, while the nongrowing tail persists but at a low population. Together, these data indicate concentration-dependent acceleration of growth kinetics and an increasing dominance of high-growth particles at elevated concentration levels.

The growth rate of the FFA-EtOH system increased with increasing concentrations, ranging from 1.1 to 3.2 nm/s. As the concentration increased, the number of particles decreased (Figure S3). Using SAM, the number of detected particles was approximately 40 for all experiments due to low contrast. Both growth rate assessment methodologies (manual and automated) demonstrated nominally identical linear growth profiles as the particle diameter increased over time for the EtOH system. The figures demonstrate tight clustering of data points on lines of fit, indicating linear kinetics independent of concentration (Figures 8 and 4). These results suggest that within this concentration range, the ethanol system exhibits stable crystallization kinetics, likely governed by consistent solute−solvent interactions and independent of solute concentration.

Within the FFA-IPA system, the particles grow linearly but finish smaller as concentration rises (10 → 15 → 20 mM). Higher FFA concentrations trigger more nucleation under the beam, intensifying competition between growing nuclei for solute molecules, causing earlier depletion, and impinging growth to larger particle sizes. The automated tracking yields a linear slope ∼0.9 nm s^{-1} for the median cohort and ∼1.1 nm s^{-1} for the fastest growing population at 10 mM (Figure 9a,d). At 10 mM, the particle size reaches to ∼300 nm by 150 s with 90% of the population remaining below this size distribution. At 15 mM, particle formation becomes more rapid (Figure 9b,e), with particles reducing in size to ∼250 nm in diameter at 150 s. The median fitted growth rates are ∼0.8 nm s^{-1} and ∼2.2 nm s^{-1} for the fastest growing population. At 20 mM, the highest number of crystals are observed (Figure 9f), with the smallest size, overall median size decreases to 180 nm or smaller at 150 s. The linear fit of the growth rates at 20 mM gives a median growth rate ∼0.7 nm s^{-1} with the fastest growing population growing at a rate of ∼1.2 nm s^{-1}.

The average particle sizes at 20 mM (highest IPA concentration in this study) were around a few hundred nanometers, smaller than in the ethanol system. The growth rate of the medium-sized particles decreased with an increasing concentration (0.9, 0.8, and 0.7 nm/s). The size distribution remained similar across different concentrations. As the concentration increased, the number of particles in the image also increased. From SAM, the number of detected particles was about 200 for all experiments in IPA (Figure S4). FFA crystallization behavior in IPA through increasing concentrations (10 mM, 15 mM, and 20 mM) shows a clear concentration-dependent enhancement in growth dynamics. At higher concentrations, particle growth slows, but the quantity of particles increases, indicating more nucleation. This suggests that the FFA-IPA system is highly sensitive to solute concentration, with availability of molecules and localized supersaturation contributing to more intensive and quicker crystallization at higher concentrations as evident from Figure 5.

In short, growth kinetics derived from manual measurements reflect growth rate analysis of single particles, whereas those from the automated measurements more accurately reflect the growth rate of the population. Additionally, the growth rate trends agree between the manual and automated approaches, i.e., for the EtOH solutions, the growth rate increases with solute concentration, and for IPA solutions, the growth rate decreases with increasing solute concentrations. This confirms that the manual approach is a reliable benchmark, validating the automated approach. More importantly, the automated technique quantifies population heterogeneity, from growing to nongrowing particles that single-trajectory analyses cannot resolve. Together, these complementary approaches provide both accuracy and statistical breadth, strengthening the robustness of our growth rate estimates and the inferences that can be drawn from them.

4. CONCLUSIONS

This body of work investigates the crystallization of FFA solutions at concentrations far below bulk saturation, revealing pathways that fall outside classical, supersaturation-driven frameworks. Key findings reveal that nucleation in ethanol (EtOH) is rapid at low electron flux densities (EFD ∼ 1 $e^-/Å^2/s$), with visible nuclei forming in approximately 15 s. Conversely, isopropanol (IPA) necessitates a higher flux (∼10 $e^-/Å^2/s$) and longer exposure times (∼120 s) to achieve similar nucleation outcomes. Importantly, despite operating in a nonequilibrium and radiolysis-affected environment, the study preserves fundamental thermodynamic trends, with induction times decreasing as concentration increases.

The LPTEM experiments demonstrate the governing role of solute concentration in the crystallization process, even under undersaturated conditions. Variations in crystal size and induction time were attributed to distinct nucleation kinetics, morphology, and growth characteristics inherent to each solvent. Notably, above ∼10 mM, both solvents formed predominantly faceted/hexagonal crystals resembling Form I. Below this threshold, EtOH produced nanoparticles and

https://doi.org/10.1021/acs.cgd.6c00030
Cryst. Growth Des. 2026, 26, 6261−6273

clusters, while IPA displayed mesoscale clusters with hints of faceting. This is indicative of nonclassical crystallization in both EtOH and IPA.

Crystals exhibited larger sizes within the electron beam area compared to unirradiated regions, suggesting that localized radiolysis fosters supersaturation and facilitates the diffusion of reactive species leading to the crystallization of smaller crystals outside the beam. The collective data highlight the intricate interplay between electron doses, solvent properties, and radiolysis in modulating nucleation and growth, favoring the emergence of a metastable hexagonal Form I polymorph.

The analyses reveal that in EtOH, growth per particle increases with concentration in both manual and automated measurements, maintaining a roughly linear relationship over time. In contrast, for IPA, the growth rate diminishes with concentration due to increased nucleation rates leading to solute competition and diffusion limitations for growth. Although manual growth rate measurements yield higher values than automated analyses, both approaches demonstrate consistent trends. This supports the interpretation that local supersaturation, influenced by beam conditions and solute−solvent interactions, dictates whether crystallization occurs in a supply rich, continually growing regime (EtOH) or a competition-dominated, diffusion-limited phase (IPA). Conclusively, it can be said that the manual growth rate measurement is a more selective and tedious approach, whereas the automated approach is a more statistical technique to analyze the growth patterns.

In summary, this study shows how electron fluxes, solvent characteristics, and radiolytic events collaboratively dictate the nucleation and growth behavior of organic compounds like FFA. This work positions LPTEM as a versatile technique for elucidating nanoscale crystallization processes, with significant implications for polymorph selection and process optimization in pharmaceutical applications.

■ ASSOCIATED CONTENT

Supporting Information

The Supporting Information is available free of charge at https://pubs.acs.org/doi/10.1021/acs.cgd.6c00030.

Supporting Information Document (DOCX)

Video S1: LPTEM in situ recording of solvent displacement from the viewing window upon electron flux >10 $e^-/Å^2/s$. Rapid bubble formation and thinning of liquid layer are observed, indicating evaporation driven by beam-induced heating and radiolysis. System: FFA-EtOH (MP4)

Video S2: LPTEM video capturing a marked contrast shift as the solvent exits the viewing window at electron flux >10 $e^-/Å^2/s$. The disappearance of the liquid phase is evidenced by increased image sharpness and reduced dynamic scattering, confirming solvent loss due to beam exposure. (MP4)

Video S3: Additional LPTEM video capturing a marked contrast shift as the solvent exits the viewing window at electron flux >10 $e^-/Å^2/s$. (MP4)

Video S4: LPTEM video capturing multiple crystal growth events in a 10 mM FFA solution in EtOH under an electron flux of 1 $e^-/Å^2/s$. (MP4)

Video S5: LPTEM video capturing crystal growth in a 100 mM FFA solution in EtOH under an electron flux of 1$e^-/Å^2/s$. The video shows the dynamic nucleation and growth processes occurring within the solution under continuous electron irradiation (MP4)

Video S6: LPTEM video showing the nucleation of a 20 mM FFA solution in IPA under an electron flux of 10 $e^-/Å^2/s$. The video shows nucleation and crystal growth under continuous electron beam irradiation (MP4)

Video S7: LPTEM video showing the nucleation of a 15 mM FFA solution in IPA under an electron flux of 10 $e^-/Å^2/s$. The video shows nucleation and crystal growth under continuous electron beam irradiation (MP4)

Video S8: LPTEM video showing the nucleation of a 10 mM FFA solution in IPA under an electron flux of 10 $e^-/Å^2/s$. The video shows nucleation and crystal growth under continuous electron beam irradiation (MP4)

Video S9: LPTEM video showing the movement of low-concentration clusters in a 1 mM FFA solution in EtOH under an electron flux of 1 $e^-/Å^2/s$. The video captures the dynamic behaviour and mobility of small aggregates over time under continuous electron irradiation (MP4)

Video S10: LPTEM video showing the interaction of low-concentration clusters in a 1 mM FFA solution in EtOH under an electron flux of 1 $e^-/Å^2/s$. The video captures two clusters approaching and joining over time under continuous electron irradiation (MP4)

Video S11. Under prolonged electron beam irradiation at an electron flux of 10 $e^-/Å^2/s$, the initially formed FFA crystals in the 20 mM FFA solution in IPA exhibit structural degradation, likely due to solvent displacement and the limited beam resilience of the solvent. This observation highlights the importance of carefully controlling the exposure time during LPTEM experiments to preserve crystal integrity and obtain reliable structural information (MP4)

■ AUTHOR INFORMATION

Corresponding Author

Jennifer Cookman − *Department of Chemical Sciences, University of Limerick, Limerick V94 T9PX, Ireland; Department of Physics and SSPC the Research Ireland Centre for Pharmaceuticals, Bernal Institute, University of Limerick, Limerick V94 T9PX, Ireland;* orcid.org/0000-0002-7054-7322; Email: Jennifer.Cookman@ul.ie

Authors

Sara Fatima − *Department of Chemical Sciences, University of Limerick, Limerick V94 T9PX, Ireland; SSPC the Research Ireland Centre for Pharmaceuticals, Bernal Institute, University of Limerick, Limerick V94 T9PX, Ireland;* orcid.org/0009-0005-9775-6326

Junbeom Park − *Institute of Energy Technologies - Fundamental Electrochemistry (IET-1), Forschungszentrum Jülich GmbH, 52428 Jülich, Germany;* orcid.org/0000-0003-2548-2985

Govind Ummethala − *Ernst-Ruska Centre for Microscopy and Spectroscopy with Electrons, Forschungszentrum Jülich GmbH, 52428 Jülich, Germany*

Shibabrata Basak − *Institute of Energy Technologies - Fundamental Electrochemistry (IET-1), Forschungszentrum Jülich GmbH, 52428 Jülich, Germany;* orcid.org/0000-0002-4331-4742

Rüdiger-A. Eichel − *Institute of Energy Technologies - Fundamental Electrochemistry (IET-1), Forschungszentrum*

https://doi.org/10.1021/acs.cgd.6c00030
Cryst. Growth Des. 2026, 26, 6261−6273

Jülich GmbH, 52428 Jülich, Germany; orcid.org/0000-0002-0013-6325

Amir Tavabi − *Ernst-Ruska Centre for Microscopy and Spectroscopy with Electrons, Forschungszentrum Jülich GmbH, 52428 Jülich, Germany;* orcid.org/0000-0003-1551-885X

Rafal Dunin Borkowski − *Ernst-Ruska Centre for Microscopy and Spectroscopy with Electrons, Forschungszentrum Jülich GmbH, 52428 Jülich, Germany;* orcid.org/0000-0001-8082-0647

Sarah Hudson − *Department of Chemical Sciences, University of Limerick, Limerick V94 T9PX, Ireland; SSPC the Research Ireland Centre for Pharmaceuticals, Bernal Institute, University of Limerick, Limerick V94 T9PX, Ireland;* orcid.org/0000-0002-6718-2190

Complete contact information is available at: https://pubs.acs.org/10.1021/acs.cgd.6c00030

Author Contributions

Conceptualisation, S.F., S.H. and J.C.; solubility and crystallization, S.F.; recorded and analyzed the LPTEM images and videos, S.F. and J.C.; original draft, writing, reviewing, and editing, S.F., S.H. and J.C.; funding acquisition, S.F. and J.C.; supervision, S.H. and J.C.

Funding

Research Ireland funding 21/PATH-S/9315 and 12/RI/2345/SOF are gratefully acknowledged for support of this research.

Notes

The authors declare no competing financial interest.

■ ACKNOWLEDGMENTS

This work was supported by the Research Ireland (formerly SFI) and Department of Chemical Sciences along with Bernal Institute at the University of Limerick. S.F. would like to acknowledge Microscopy Society of Ireland (MSI), the Royal Society of Chemistry (RSC), the Solid State Chemistry Group (SSCG), and the Royal Microscopical Society (RMS) for scholarships to present this work at the Gordon Research Conference (GRC) in Tuscany, Italy, Microscopy and Microscience Congress (MMC) in Manchester, UK, and International Symposium on Industrial Crystallization (ISIC), Glasgow, Scotland. The authors gratefully acknowledge the use of resources in the "ER-C 2.0" National Research Infrastructure for High-Resolution Electron Microscopy in Forschungszentrum Jülich GmbH.

■ REFERENCES

(1) Gao, Z.; Rohani, S.; Gong, J.; Wang, J. Recent Developments in the Crystallization Process: Toward the Pharmaceutical Industry. *Engineering* **2017**, *3*, 343−353.

(2) Bučar, D.; Lancaster, R. W.; Bernstein, J. Verschwundene Polymorphe: eine Neubetrachtung. *Angew. Chem.* **2015**, *127*, 7076−7098.

(3) Cheuk, D.; Zeglinski, J.; Krishnaraj, R.; Rasmuson, Å. C. Influence of solvent on crystal nucleation of benzocaine. *CrystEngComm* **2020**, *22*, 8330−8342.

(4) Meenan, P. A.; Anderson, S. R.; Klug, D. L. The Influence of Impurities and solvents on Crystallization. In *Handbook of Industrial Crystallization*; Allan, S., Myerson, Eds.; Butterworth-Heinemann: Boston, 2002; pp 67−100.

(5) Mullin, J. W.; Söhnel, O. Expressions of supersaturation in crystallization studies. *Chem. Eng. Sci.* **1977**, *32*, 683−686.

(6) Zaykovskaya, A.; Louhi-Kultanen, M. Cooling and Evaporative Crystallization of α-D-Galactose from a Highly Viscous Industrial Side Stream. *Chem. Eng. Technol.* **2023**, *46*, 2330−2336.

(7) Nagy, Z. K.; Steele, G. Supersaturation and direct nucleation control of an industrial pharmaceutical crystallisation process using a crystallisation process informatics system. In *Proceedings of the International Workshop on Industrial Crystallization*: Delft, The Netherlands, 2011, pp 7−9.

(8) Zhang, D.; Xu, S.; Du, S.; Wang, J.; Gong, J. Progress of Pharmaceutical Continuous Crystallization. *Engineering* **2017**, *3* (3), 354−364.

(9) Chen, J.; Sarma, B.; Evans, J. M. B.; Myerson, A. S. Pharmaceutical crystallization. *Cryst. Growth Des.* **2011**, *11*, 887−895.

(10) Fda *Guidance for Industry ANDAs: Pharmaceutical Solid Polymorphism Chemistry, Manufacturing, and Controls Information*, 2007.

(11) Fda, C.; Stewart, F. *Regulatory Classification of Pharmaceutical Co-Crystals Guidance for Industry*, 2018.

(12) Mullin, J. W. 5—Nucleation. In *Crystallization*; Elsevier Science & Technology: Oxford: Butterworth-Heinemann, 2001; Vol. *5*, pp 181−214.

(13) Myerson, A. S.; Ginde, R. 2—Crystals, crystal growth, and nucleation. In *Handbook of Industrial Crystallization*, 2 ed.; Butterworth-Heinemann, 2002; pp 33−65..

(14) Mullin, J. W. 6—Crystal Growth. In *Crystallization*; Elsevier Science and Technology, Butterworth-Heinemann, Oxford, 2001; Vol. *5*, pp 216−284.

(15) Lutsko, J. F.; Durán-Olivencia, M. A. Classical nucleation theory from a dynamical approach to nucleation. *J. Chem. Phys.* **2013**, *138*, 244908.

(16) Karthika, S.; Radhakrishnan, T. K.; Kalaichelvi, P. A Review of Classical and Nonclassical Nucleation Theories. *Cryst. Growth Des.* **2016**, *16*, 6663−6681.

(17) Cookman, J.; Hamilton, V.; Hall, S. R.; Bangert, U. Non-classical crystallisation pathway directly observed for a pharmaceutical crystal via liquid phase electron microscopy. *Sci. Rep.* **2020**, *10*, 19156.

(18) Cookman, J.; Hamilton, V.; Price, L. S.; Hall, S. R.; Bangert, U. Visualising early-stage liquid phase organic crystal growth: Via liquid cell electron microscopy. *Nanoscale* **2020**, *12*, 4636−4644.

(19) Woehl, T. J.; Abellan, P. Defining the radiation chemistry during liquid cell electron microscopy to enable visualization of nanomaterial growth and degradation dynamics. *J. Microsc.* **2017**, *265*, 135−147.

(20) Fritsch, B.; Malgaretti, P.; Harting, J.; Mayrhofer, K. J. J.; Hutzler, A. Precision of Radiation Chemistry Networks: Playing Jenga with Kinetic Models for Liquid-Phase Electron Microscopy. *Precis. Chem.* **2023**, *1*, 592−601.

(21) Vratsanos, M. A. *Situ Morphology, Formation, and Dynamics of Heterogeneous Soft Matter Systems Elucidated via Liquid Phase Transmission Electron Microscopy*. Northwestern University Theses, 2023.

(22) López-Mejías, V.; Kampf, J. W.; Matzger, A. J. Nonamorphism in flufenamic acid and a new record for a polymorphic compound with solved structures. *J. Am. Chem. Soc.* **2012**, *134*, 9872−9875.

(23) Nechipadappu, S. K.; Tekuri, V.; Trivedi, D. R. Pharmaceutical Co-Crystal of Flufenamic Acid: Synthesis and Characterization of Two Novel Drug-Drug Co-Crystal. *J. Pharm. Sci.* **2017**, *106*, 1384−1390.

(24) Du, J. S.; Bae, Y.; De Yoreo, J. J. Non-classical crystallization in soft and organic materials. *Nat. Rev. Mater.* **2024**, *9*, 229−248.

(25) Li, H.; Wen, H.; Stowell, J. G.; Morris, K. R.; Byrn, S. R. Crystal quality and physical reactivity in the case of flufenamic acid (FFA). *J. Pharm. Sci.* **2010**, *99*, 3839−3848.

(26) Ravi, N.; et al. SAM 2: Segment Anything In Images And Videos. *arXiv* **2024**, arXiv: 2408.00714.

(27) Alshehri, S.; Shakeel, F. Solubility measurement, thermodynamics and molecular interactions of flufenamic acid in different neat solvents. *J. Mol. Liq.* **2017**, *240*, 447−453.

(28) Schneider, N. M.; et al. Electron-Water interactions and implications for liquid cell electron microscopy. *J. Phys. Chem. C* **2014**, *118*, 22373−22382.
(29) Koo, K.; et al. Radiation Chemistry in Environmental Transmission Electron Microscopy. *ACS Nano* **2025**, *19*, 10369−10380.
(30) Simic, M.; Neta, P.; Hayon, E. Pulse radiolysis study of alcohols in aqueous solution. *J. Phys. Chem.* **1969**, *73* (11), 3794−3800.
(31) Hayon, E.; Weiss, J. J., 772 The chemical action of ionising radiations on simple aliphatic alcohols. Part I. Irradiation of ethanol in the liquid and in the solid state and in the presence of solutes. *J. Chem. Soc.* **1961**, 3962−3970.
(32) Korpanty, J.; Parent, L. R.; Gianneschi, N. C. Enhancing and Mitigating Radiolytic Damage to Soft Matter in Aqueous Phase Liquid-Cell Transmission Electron Microscopy in the Presence of Gold Nanoparticle Sensitizers or Isopropanol Scavengers. *Nano Lett.* **2021**, *21*, 1141−1149.
(33) Burr, J. G.; Strong, J. D. Radiolysis of the Benzophenone-Propanol-2 System the radiolysis of organic solutions II. In *The Benzophenone-Propanol-2 System 1*; Atomics International, 1959.
(34) Gebauer, D.; Raiteri, P.; Gale, J. D.; Cölfen, H. On classical and non-classical views on nucleation. *Am. J. Sci.* **2018**, *318*, 969−988.
(35) Gebauer, D.; Kellermeier, M.; Gale, J. D.; Bergström, L.; Cölfen, H. Pre-nucleation clusters as solute precursors in crystallisation. *Chem. Soc. Rev.* **2014**, *43*, 2348−2371.
(36) Jehannin, M.; Rao, A.; Cölfen, H. New Horizons of Nonclassical Crystallization. *J. Am. Chem. Soc.* **2019**, *141*, 10120−10136.
(37) Khamar, D.; Zeglinski, J.; Mealey, D.; Rasmuson, Å. C. Investigating the Role of Solvent−Solute Interaction in Crystal Nucleation of Salicylic Acid from Organic Solvents. *J. Am. Chem. Soc.* **2014**, *136*, 11664−11673.
(38) Pang, Y.; Gaisford, S.; Magdysyuk, O. V.; Williams, G. R. Polymorphic transitions in flufenamic acid-trehalose composites. *Int. J. Pharm.: X* **2023**, *6*, 100200.
(39) Fritsch, B.; Lee, S.; Körner, A.; Schneider, N. M.; Ross, F. M.; Hutzler, A. The Influence of Ionizing Radiation on Quantification for In Situ and Operando Liquid-Phase Electron Microscopy. *Adv. Mater.* **2025**, *37*, 2415728.
(40) Fritsch, B.; et al. Accessing local electron-beam induced temperature changes during: In situ liquid-phase transmission electron microscopy. *Nanoscale Adv.* **2021**, *3*, 2466−2474.
(41) Mullin, J. W. Solutions and Solubility. *Crystallization* **2001**, 86−134.
(42) Voorhees, P. W. The Theory of Ostwald Ripening. *J. Stat. Phys.* **1985**, *38*, 231−252.

https://doi.org/10.1021/acs.cgd.6c00030
Cryst. Growth Des. 2026, 26, 6261−6273